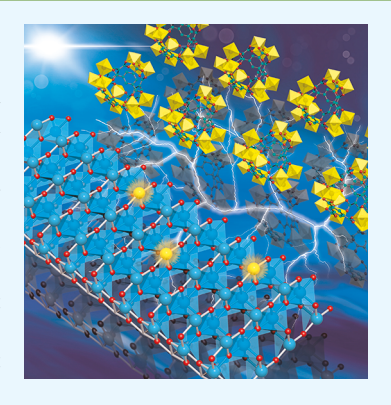
**♦ Cite This:** ACS Appl. Mater. Interfaces 2019, 11, 12516−12524

# Mechanistic Insight into Photocatalytic Pathways of MIL-100(Fe)/ TiO<sub>2</sub> Composites

Xiang He,<sup>†</sup> Hong Fang,<sup>‡</sup> David J. Gosztola, <sup>§</sup> Zhang Jiang, <sup>||</sup> Puru Jena, <sup>‡</sup> and Wei-Ning Wang\*, <sup>†</sup>

Supporting Information

ABSTRACT: The integration of metal-organic frameworks (MOFs) with semiconductors has attracted mounting attention for photocatalytic applications. However, more efforts are needed to unravel the interface structure in MOF/semiconductor composites and its role in charge transfer. Herein, a MIL-100(Fe)/TiO<sub>2</sub> composite was synthesized as a prototypical photocatalyst and studied systematically to explore the interface structure and unravel the charge transfer pathways during the photocatalytic processes. The composite was fabricated by growing MIL-100(Fe) crystals on TiO<sub>2</sub> using surface-coated FeOOH as the precursor. The as-prepared MIL-100(Fe)/TiO<sub>2</sub> exhibited significantly improved photocatalytic performance over pristine TiO2, which was mainly because of the enhanced charge separation as confirmed by transient absorption spectroscopy analysis. This enhancement partially arose from the special chemical structure at the interface, where the Fe-O-Ti bond was formed. As verified by the density functional theory calculation, this distinct structure would create defect energy levels adjacent to the valence band maximum of TiO<sub>2</sub>.



During the photocatalytic processes, the defect energy levels serve as sinks to capture excited charge carriers and retard the recombination, which subsequently leads to the increased charge density and promoted photocatalytic efficiency. Meanwhile, the intimate interactions between MIL-100(Fe) and TiO<sub>2</sub> would also help to improve the charge separation by transferring photo-induced holes through the ligands to Fe-O clusters. These findings would advance the fundamental understanding of the interface structure and the charge transfer pathways in MOF/semiconductor composite photocatalysts.

KEYWORDS: metal-organic framework, photocatalysis, charge transfer, transient absorption spectroscopy, defect energy level

## ■ INTRODUCTION

Metal-organic frameworks (MOFs), an attractive class of porous crystals assembled from metal ions/clusters and organic linkers, have drawn intense interest because of their distinguished properties, including huge surface areas, tailorable chemistries, and tunable cavities. 1-4 Endowed with such unique features, MOFs are promising candidates for diverse applications, including sensing,<sup>5</sup> gas separation,<sup>6,7</sup> and <sup>9</sup> In addition, the functions of MOFs can be expanded and promoted through rational integration with other components, such as metals and semiconductors. 10-13

For instance, numerous MOF-based composites have been designed and used as photocatalysts,  $^{14}$  including ZIF-8/TiO<sub>2</sub>,  $^{15}$  ZIF-8/ZnO,  $^{16}$  UiO-66/C<sub>3</sub>N<sub>4</sub>,  $^{17}$  UiO-66-NH<sub>2</sub>/Cd<sub>0.2</sub>Zn<sub>0.8</sub>S,  $^{18}$  NH<sub>2</sub>-MIL-125(Ti)/TiO<sub>2</sub>,  $^{19,20}$  MIL-125(Ti)/ and HKUST-1/TiO<sub>2</sub>, <sup>22</sup>, <sup>23</sup> where the composites exhibited significantly improved catalytic performance as compared with the individual components. Mostly, the semiconductor serves as the major catalyst, while the MOF functions as the cocatalyst or support, which promotes the catalytic efficiency by enhancing molecule adsorption and charge transfer. For instance, CdS-embedded MIL-101 demonstrated a higher ability in hydrogen evolution as

compared with either bare CdS or MIL-101.<sup>24</sup> The improved efficiency was primarily ascribed to the huge surface area of MIL-101, which not only allows the wide dispersion of CdS but also offers massive active sites. Recently, Panneri et al.<sup>25</sup> fabricated C<sub>3</sub>N<sub>4</sub>-anchored ZIF-8 composites with a highly stable micro-meso porous structure, which could adsorb up to 45% of tetracycline in its solution and achieve significantly high photodegradation efficiency. In addition to the promoted molecule adsorption, another key impetus for the enhanced photocatalytic efficiency of such MOF/semiconductor composites is the increased charge carrier density because of the distinct interface structure. For instance, Zeng et al. 15 developed a ZIF-8/TiO2 composite by incorporating ZIF-8 on TiO<sub>2</sub> nanofibers. The composite showed great improvements in photodegradation of rhodamine B mainly because of the reduced charge recombination through the N-Ti-O bonds formed at the interface between ZIF-8 and TiO2. In addition, the UiO-66/C<sub>3</sub>N<sub>4</sub> heterojunction was synthesized by Wang et al., <sup>17</sup> where the rate of H<sub>2</sub> evolution was promoted to

Received: January 7, 2019 Accepted: March 13, 2019

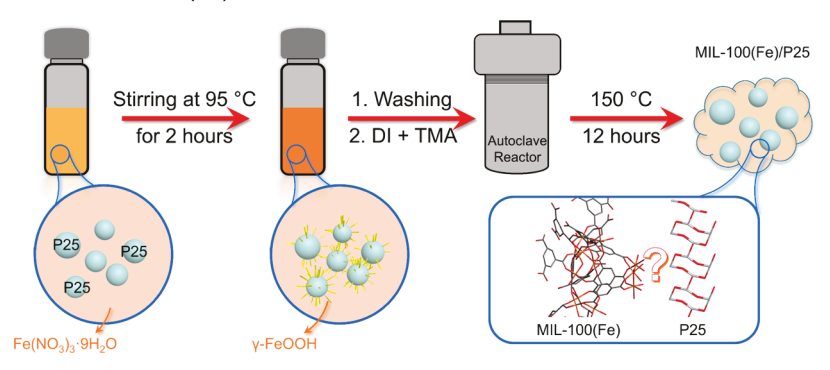
Published: March 13, 2019



<sup>&</sup>lt;sup>†</sup>Department of Mechanical and Nuclear Engineering and <sup>‡</sup>Department of Physics, Virginia Commonwealth University, Richmond, Virginia 23219, United States

 $<sup>^{\$}</sup>$ Center for Nanoscale Materials and  $^{\|}$ Advanced Photon Source, Argonne National Laboratory, Lemont, Illinois 60439, United

Scheme 1. Synthesis Process of MIL-100(Fe)/P25



17 times that of pristine C<sub>3</sub>N<sub>4</sub>. Such a huge enhancement was also attributable to the efficient interface charge transfer, as evidenced by the quenched photoluminescence (PL) emission peak and shortened PL lifetime. The interface charge transfer was also proposed to exist in MIL-100(Fe)/TiO<sub>2</sub><sup>26</sup> and ZIF-8/ C<sub>3</sub>N<sub>4</sub>.<sup>25</sup> As demonstrated by these prior studies, the distinct MOF/semiconductor interface plays a vital role in enhancing the charge transfer. However, exploration of the mechanistic basis is still in its infancy. For example, the interface structures of various MOF/semiconductor composites may differ from each other, which might lead to distinctive charge transfer pathways. To further improve the photocatalytic efficiency and fully exploit the benefits of these MOF-based composites, greater efforts should be devoted to resolving the interface structure and understanding the charge transfer pathways.

Herein, a MIL-100(Fe)/TiO<sub>2</sub> composite was used as a prototype for the study of charge transfer by using both experimental and theoretical methods. To be specific, MIL-100(Fe) was grown on the surface of TiO<sub>2</sub> (i.e., P25, Degussa (Evonik)) using the surface-coated FeOOH as the precursor (Scheme 1). The composite was then subjected to systematic material characterization and photocatalytic analysis. The results show that the MIL-100(Fe)/TiO<sub>2</sub> composite photocatalyst exhibits significantly improved performance in both degradation of tetracycline and Cr(VI) reduction than the bare TiO<sub>2</sub>, thanks to the enhanced charge separation. To unravel the underlying mechanism, systematic experiments and theoretical calculations were conducted. It was found that the enhanced charge separation arose from the defect energy levels existed in the TiO2 band structure, which were created through the partial substitution of Ti by Fe during the synthesis of MIL-100(Fe) crystals on the surface of TiO<sub>2</sub>. The outcome of this work should be able to provide new insights into the MOF/semiconductor interface structure and charge transfer, and ultimately to advance the fundaments in photocatalysis by using MOF/semiconductor composites.

## MATERIALS AND METHODS

Synthesis of MIL-100(Fe)/P25 Composites. In a typical synthesis procedure (Scheme 1), 0.025 g of P25 (Degussa (Evonik)) was first mixed with 5–40 mmol/L  $Fe(NO_3)_3 \cdot 9H_2O$  aqueous solution in a glass vial. Then, the vial was heated and stirred by a hotplate stirrer at 95 °C and 1200 rpm for 2 h. After that, the powders were washed by deionized (DI) water through the centrifugation/ redispersion process for five times to remove the iron residues. Subsequently, the powders were redispersed in 4.8 mL of DI water together with 0.3 g of trimesic acid (TMA). After vortex mixing, the mixtures were poured into a Teflon autoclave, which was then put in a muffle furnace at 150 °C for 12 h. After cooling, the composite samples were taken out from the autoclave and immersed in hot water

at 80 °C for 3 h to remove TMA residues. Finally, the composite products were obtained after washing with DI water through the centrifugation/redispersion process three times. The MIL-100(Fe)/ P25 composites are, hereafter, termed M/P-5(to 40), where the numbers refer to the initial molar concentrations of  $Fe(NO_3)_3 \cdot 9H_2O$ . The synthetic procedures for the pure MIL-100(Fe) crystals are detailed in the Supporting Information S1.

Material Characterization. The morphologies and inner structures of the materials were examined by a scanning electron microscope (SEM, Su-70, Hitachi) and a transmission electron microscope (TEM, JEM 1230, JEOL), respectively. The powder X-ray diffraction (PXRD) patterns were obtained by using a PANalytical X'Pert Pro MPD X-ray diffractometer. Vibration spectral analysis was conducted by using a Fourier transform infrared (FT-IR) spectrometer (Nicolet iS50, Thermo Scientific). The UV-vis spectra were recorded by using a spectrophotometer (Evolution 220, Thermo Fisher). X-ray photoelectron spectroscopy (XPS, ESCALAB 250, Thermo Fisher) was used to study the surface chemical composition. The wide-angle X-ray scattering (WAXS) measurements were performed at the 8-ID-E beamline, Advanced Photon Source (APS), Argonne National Laboratory, USA. The nitrogen adsorption-desorption isotherms were obtained by Autosorb iQ (Quantachrome Instruments).

Transient Absorption (TA) Spectroscopy. Femtosecond TA studies were carried out at the Center for Nanoscale Materials (CNM), Argonne National Laboratory, USA. Specifically, an amplified Ti:sapphire laser system was used, which produces 150 fs pulses centered at 800 nm with a repetition rate of 5 kHz. 90% of the output was directed to a TOPAS optical parametric amplifier to produce the pump pulse at 350 nm. The beam energy was set to 2  $\mu$ J with a spot size of 150  $\mu$ m diameter. The remaining 10% was used to generate probe pulse ranging from 450 to 700 nm by focusing into a sapphire window with a thickness of 2 mm.

Photodegradation of Tetracycline. The photocatalytic ability of the catalysts was first tested by the degradation of tetracycline with a 450 W Xe arc lamp (Newport Corporation). The experiments were conducted in a quartz beaker with continuous stirring. Specifically, 5 mg of catalyst was distributed into a 100 mL aqueous solution containing tetracycline (100 mg/L) and H<sub>2</sub>O<sub>2</sub> (20 µL). Before light irradiation, the suspension was stirred for 30 min to get adsorption equilibrium. After turning the light on, 3 mL of the suspension was taken out at certain intervals and then subjected to centrifugation to remove the catalysts. Subsequently, the concentration of the tetracycline was determined from the absorbance at its characteristic wavelength (i.e., 357 nm) by using the UV-vis spectrophotometer.

Photoreduction of Cr(VI). The experimental setup and analysis procedures of Cr(VI) photoreduction were the same as those of the photodegradation of tetracycline, except that potassium dichromate (10 mg/L) and methanol (35  $\mu$ L) were used instead of tetracycline and H<sub>2</sub>O<sub>2</sub>, respectively. The pH of the suspension was adjusted to 1.9 by adding sulfuric acid. After 30 min in the dark, the suspension was subjected to the light illumination, during which 1 mL of the suspension was withdrawn for test every 10 min. The Cr(VI) **ACS Applied Materials & Interfaces** 

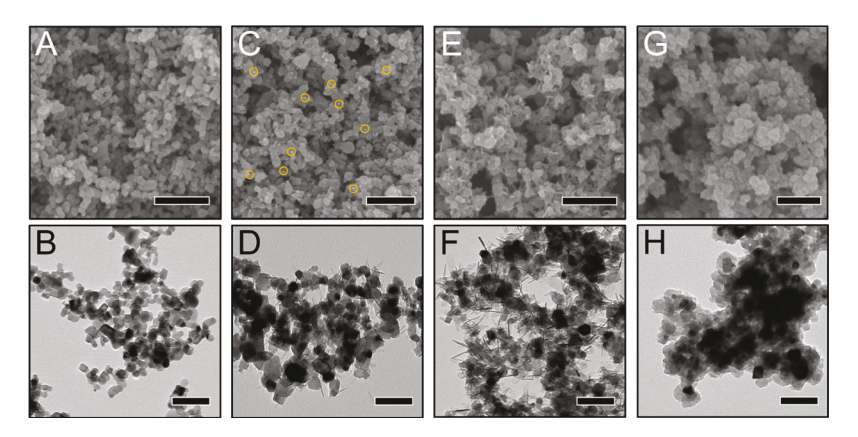


Figure 1. SEM and TEM images of pristine P25 (A,B), P25 modified by Fe(NO<sub>3</sub>)<sub>3</sub>·9H<sub>2</sub>O with various concentrations [10 (C,D) and 20 mM (E,F)], and M/P-10 (G,H), scale bars: SEM: 250 nm, TEM: 100 nm.

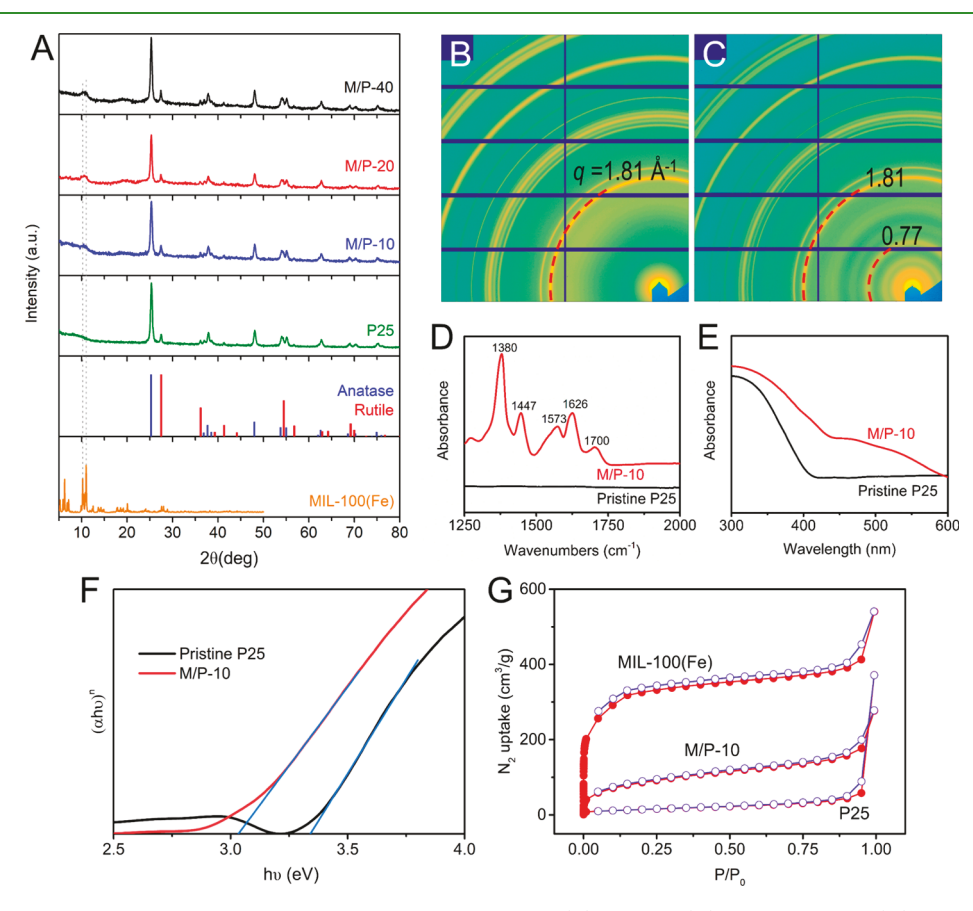


Figure 2. (A) PXRD patterns of the as-prepared samples; 2D WAXS patterns of (B) P25 and (C) M/P-10; FT-IR (D) and UV-vis spectra (E) of the samples; (F) Tauc plots of pristine P25 and M/P-10. Both samples are dominated by anatase, which has an indirect band gap. Therefore, n=2was used for both Tauc plots; and (G) nitrogen sorption isotherms at 77 K.

concentration was measured by using the diphenylcarbazide method (7196A, United States Environmental Protection Agency).

Density Functional Theory (DFT) Calculations. The DFT calculations of the electronic structures of bare TiO2 and Fe-doped TiO<sub>2</sub> were performed by using the VASP package.<sup>27</sup> The details of the calculation can be found in our prior study.

## ■ RESULTS AND DISCUSSION

Material Characterization. The morphologies and structures of the representative samples were characterized by SEM and TEM. As displayed in Figure 1A,B, pristine P25 particles are monodispersed nanocrystals with a diameter of  $\sim$ 25 nm. The surfaces of the pristine P25 nanoparticles are very smooth. After being suspended in Fe(NO<sub>3</sub>)<sub>3</sub>·9H<sub>2</sub>O aqueous solution (10 mM) and followed by stirring on a hotplate stirrer at 95 °C for 2 h, the P25 nanoparticles were decorated by some small FeOOH nanosticks on the surfaces (Figure 1C,D). Further increasing the concentration of Fe(NO<sub>3</sub>)<sub>3</sub>·9H<sub>2</sub>O led to the formation of more and longer FeOOH sticks (Figure 1E,F). Characterization of the P25/ FeOOH composite was carried out by FT-IR, where the major bands are discovered at 1020 and 1166 cm<sup>-1</sup> (Figure S2A), corresponding to the characteristic vibration of  $\gamma$ -FeOOH.<sup>29</sup> The PXRD pattern of the P25/FeOOH is shown in Figure

S2B, where all the peaks can be assigned to P25 and no apparent peaks of  $\gamma$ -FeOOH are observed, indicating the amorphous nature of the surface-coated FeOOH. Given this, the as-coated FeOOH could be used as a precursor for the facile growth of MIL-100(Fe) crystals. Specifically, the P25/FeOOH was put into TMA solution and subjected to hydrothermal synthesis to convert FeOOH to MIL-100(Fe) and obtain the MIL-100(Fe)/P25 composite. As exhibited in Figure 1G,H, the surfaces of the MIL-100(Fe)/P25 composite turn out to be very rough owing to the presence of MIL-100(Fe) as the shell. The energy dispersive X-ray spectroscopy (EDX) spectrum (Figure S3) obtained from the MIL-100(Fe)/P25 composite confirms the co-existence of Ti and Fe.

The crystallinity of the MIL-100(Fe)/P25 composites was studied by PXRD measurements. As shown in Figure 2A, pristine P25 has a main anatase phase and a trace amount of the rutile phase. With the incorporation of MIL-100(Fe), the crystalline structure of P25 was perfectly preserved, and a new diffraction peak shows up at ~10°, attributed to the crystal phase of MIL-100(Fe). 30 The intensity of this new diffraction peak increases with the increased amount of MIL-100(Fe) in the composite. In addition to the PXRD patterns, 2D WAXS patterns of the samples were also obtained. As shown in Figure 2B, the pristine P25 powders exhibit ring patterns with q >1.81 Å<sup>-1</sup>. With the presence of MIL-100(Fe), new ring patterns emerged with  $q < 1.81 \text{ Å}^{-1}$  (Figure 2C), which originated from the crystal structure and porosity of MIL-100(Fe) crystals. For instance, the ring pattern at the position of q = 0.77 Å<sup>-1</sup> comes from the repeating structure with a dimension of 8.2 Å, which is the pore window size of the MIL-100(Fe) crystals. The MIL-100(Fe) component in the MIL-100(Fe)/P25 composite was also supported by the FT-IR results. As revealed in Figure 2D, no vibrational peaks were observed for the pristine P25 from 1250 to 2000 cm<sup>-1</sup>. While, for the MIL-100(Fe)/P25 composite, several peaks were observed at 1380, 1447, 1573, 1626, and 1700 cm<sup>-1</sup>, which can be ascribed to carboxylate groups on the surface of MIL-100(Fe).31 The optical properties of the samples were evaluated by the UV-vis measurements. As shown in Figure 2E, the pristine P25 exhibits absorption of UV light (<400 nm). After the incorporation of MIL-100(Fe), the light absorption extends to the visible light range (<600 nm), indicating the enhanced light absorption of the MIL-100(Fe)/ P25 composites. Tauc plots (Figure 2F) were derived from the UV-vis spectra to calculate the band gaps. As displayed in Figure 2F, the band gaps of P25 and M/P-10 were determined to be 3.34 and 3.03 eV, respectively. Evidently, the incorporation of MIL-100(Fe) narrows down the band gap, which would boost the light utilization during the photocatalytic processes. The Brunauer-Emmett-Teller surface areas were determined from the N2 sorption isotherms (Figure 2G). More specifically, the surface area of pristine P25 was determined to be  $53 \text{ m}^2/\text{g}$ . While, for M/P-10, the surface area was improved to  $307 \text{ m}^2/\text{g}$  because of the incorporation of high-quality MIL-100(Fe) crystals (Supporting Information S1, 1189 m<sup>2</sup>/g).

Photocatalytic Performance. The photocatalytic abilities of the MIL-100(Fe)/P25 composites were evaluated through both photooxidation and photoreduction experiments as detailed below. The oxidation ability of the samples was analyzed by tetracycline degradation. As shown in Figure 3A, both pristine P25 and MIL-100(Fe)/P25 composites exhibited

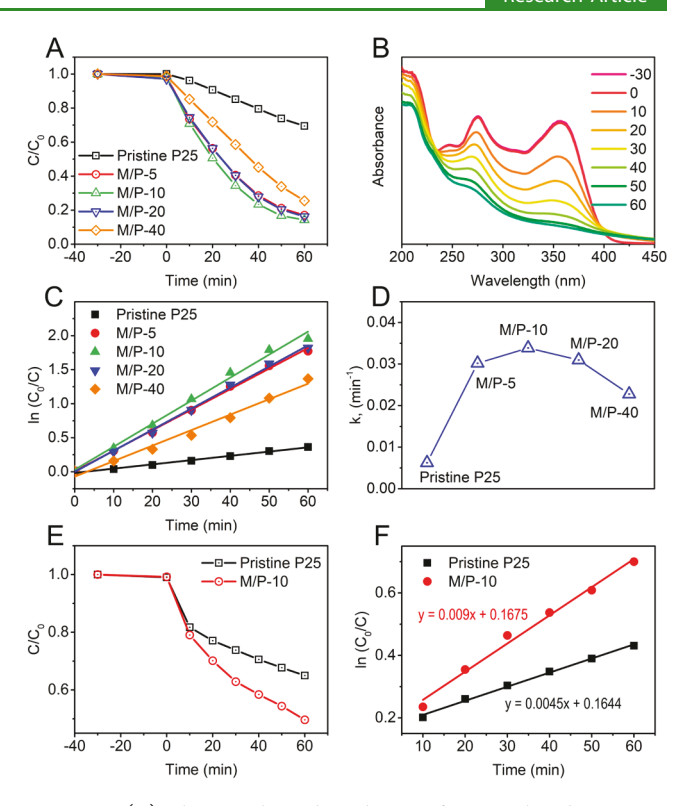


Figure 3. (A) Photocatalytic degradation of tetracycline by pristine P25 and the as-prepared MIL-100(Fe)/P25 composites; (B) UV—vis spectra of tetracycline degraded by M/P-10 (time unit: min); the pseudo-first-order kinetic plots (C) and the corresponding reaction rate constants (D) of tetracycline degradation over various photocatalysts; (E) Cr(VI) reduction by pristine P25 and M/P-10; and (F) the pseudo-first-order kinetic plots for the Cr(VI) reduction.

weak adsorption abilities toward tetracycline, as the minimal decrease was observed in the concentration of tetracycline after 30 min mixing in the dark. As expected, the MIL-100(Fe)/P25 composites show better performance than the pristine P25 in the photodegradation of tetracycline. Specifically, only 30.5% of tetracycline was degraded by pristine P25 after 60 min light irradiation. However, the degradation efficiency was enhanced to 83.0, 85.8, 83.8, and 74.5% by M/P-5, -10, -20, and -40, respectively. Notably, the amount of MIL-100(Fe) in the composite system plays an important role in the photodegradation efficiency. Initially, the photodegradation efficiency was promoted with an increasing amount of MIL-100(Fe). The optimal composite was found to be M/P-10, which possesses the highest efficiency toward tetracycline photodegradation (85.8%), ~2.8 times that of P25. Whereas, a further increased MIL-100(Fe) amount is detrimental to the photocatalytic efficiency because the excessive MIL-100(Fe) would block P25, limiting the light absorption and the accessibility of the active sites of P25. The UV-vis spectra of tetracycline degraded by M/P-10 are presented in Figure 3B. It is obvious that the intensity of the characteristic absorbance peak of tetracycline at 357 nm gradually weakens with prolonged light illumination.

As exhibited in Figure 3C, the tetracycline degradation follows pseudo-first-order kinetics

$$\ln\left(\frac{C_0}{C}\right) = kt$$
(1)

where  $C_0$  and C are the concentrations of tetracycline at 0 min and a given time (t), respectively, and k is the apparent firstorder rate constant  $(\min^{-1})$ . The values of k are displayed in Figure 3D, where the largest rate constant for degradation of tetracycline obtained by M/P-10 was calculated to be 0.0339 min<sup>-1</sup>, which is 5.38 times that by the pristine P25 (0.0063  $min^{-1}$ ).

In addition, the incorporation of MIL-100(Fe) with TiO<sub>2</sub> also facilitates photocatalytic reduction ability of the composite, as demonstrated by Cr(VI) reduction. As shown in Figure 3E, with MIL-100(Fe), the percentage of reduced Cr(VI) was improved from 35 to 50%. The photocatalytic reduction of Cr(VI) also fits the pseudo-first-order kinetic (Figure 3F), and the reaction rate constant obtained by M/P-10 (i.e., 0.009) was found to be twice of that by pristine P25 (i.e., 0.0045).

Mechanism Exploration. The pathways of the photocatalytic degradation of tetracycline and reduction of Cr(VI) have been discussed in prior literatures. 21,32-34 In brief, there are several steps involved in the photocatalytic process, including molecule adsorption, light absorption, charge separation and transfer, and subsequent redox reactions. In the case of photodegradation of tetracycline, the photogenerated electrons would be consumed by H2O2 and dissolved  $O_2$  to generate OH and  $O_2^{\bullet -}$ , respectively. Meanwhile, holes would react with water to produce OH. All these oxidative species (i.e.,  $h^+$ ,  ${}^{\bullet}OH$  and  $O_2^{\bullet-}$ ) would degrade the tetracycline to fulvic acid- or humic acid-like substances, which would be ultimately mineralized into CO<sub>2</sub> and H<sub>2</sub>O.<sup>21</sup> On the other hand, the Cr(VI) was primarily reduced to Cr(III) by the photo-induced electrons,<sup>33</sup> while holes were consumed by the hole scavenger (i.e., methanol). The dominating steps in the above photocatalytic processes are molecule adsorption and charge separation.<sup>2</sup>

Typically, the incorporated MOF would act as a cocatalyst and improve the photocatalytic performance mainly by enhancing molecule adsorption and increasing charge carrier density. 15,26 As demonstrated in prior studies, MIL-100(Fe) crystals possess high abilities toward the adsorption of tetracycline and Cr(VI) because of the favorable pore geometry and high porosity.<sup>35–37</sup> In this study, the surfacecoated MIL-100(Fe), however, does not improve the adsorption of either tetracycline or Cr(VI) (Figure 3A,E), which suggests that only small amount of MIL-100(Fe) was incorporated in the composite system. To quantify the composition ratios of the MIL-100(Fe)/P25 composite, Rietveld refinement was performed by using the Materials Analysis Using Diffraction (MAUD) program. The results show that the weight fractions of MIL-100(Fe), anatase, and rutile in the M/P-10 are 2.8, 77.8, and 19.4 wt %, respectively. Given such a low weight fraction of MIL-100(Fe) in the composite of M/P-10, it is reasonable that the incorporation of MIL-100(Fe) exhibited minimal improvement in the adsorption of tetracycline or Cr(VI).

Based on the above discussion, the enhanced photocatalysis efficiency in the current study is mainly ascribed to the increased amount of charge carriers, which can be monitored with the aid of ultrafast TA spectroscopy analysis. The TA spectra of P25 and M/P-10 composites with a delay time of 2 ps are shown in Figure 4A. With the pump pulse of 350 nm, P25 produces negative TA signals in the spectral region of 450-750 nm because of the stimulated emission (SE) (Figure 4C), in accordance with the previously reported TA

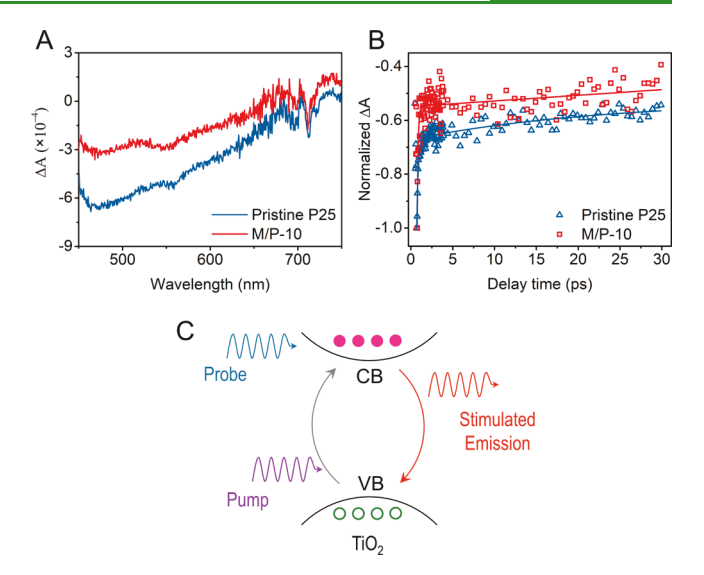


Figure 4. (A) TA spectra recorded 2 ps after the excitation pulse; (B) normalized TA kinetics probed at 465 nm; and (C) schematic illustration depicting the charge transfer during TAS measurements.

spectra<sup>23,38</sup> and the PL spectra obtained from the bare TiO<sub>2</sub>.<sup>39</sup> It should be noted that, the ground-state bleach (GSB) process also contributes to the negative TA signals, which is not the case here as GSB occurs in a much bluer region.<sup>38</sup> A similar TA spectrum is observed for M/P-10 but with a less negative signal (Figure 4A), indicating less SE, that is, fewer electrons are coming back from excited states to ground states, or in other words, less recombination of the charge carriers. The recovery of the TA signals at 465 nm (i.e., SE) for both P25 and M/P-10 shows multiexponential decay, and M/P-10 shows a faster recovery than bare P25 (Figure 4B). The TA kinetics were further analyzed by using the global analysis,<sup>4</sup> expressed as follows

$$\Delta A = \sum_{i=1}^{n} \alpha_i(\lambda) \exp\left(-\frac{t}{\tau_i}\right) \tag{2}$$

where  $\alpha_i(\lambda)$  is the pre-exponential factor at a specific wavelength and  $\tau_i$  is the corresponding lifetime. Both of  $\alpha_i(\lambda)$  and  $\tau_i$  are dependent on probe wavelength  $(\lambda)$ . According to the global analysis, the excited states of both P25 and M/P-10 decayed biexponentially. For M/P-10, the lifetimes of the SE were determined to be 119 fs and 5.63 ps, faster than those (176 fs and 22.90 ps, respectively) of the bare P25. As mentioned earlier, the SE mainly originates from the recombination of the charge carriers. Therefore, the short lifetime of the SE indicates less recombination of charge carriers in the case of M/P-10. The enhanced separation of the charge carriers might be owing to the generation of defect energy levels in the TiO2 band structure after the synthesis of MIL-100(Fe). The defect energy levels would serve as trappers of charge carriers, which would prevent them from recombination, and eventually increase the charge carrier density and lead to promoted photocatalytic efficiency.

The formation of the defect energy levels is attributable to the distinct interface structure of the MIL-100(Fe)/P25 composite, which was analyzed by XPS measurements. As displayed in Figure 5A, the XPS survey spectrum reveals that the M/P-10 composite contains Fe, Ti, O, and C elements. The high-resolution spectrum of O 1s (Figure 5B) consists of three component peaks at 531.4, 530.4, and 528.8 eV. The Fe

**ACS Applied Materials & Interfaces** 

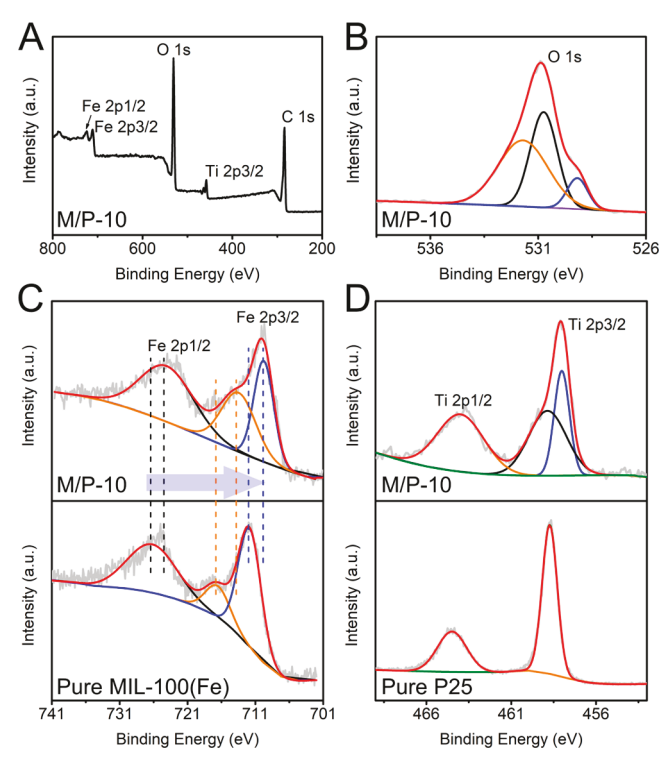


Figure 5. XPS spectra: (A) survey scan; high-resolution spectra of (B) O 1s, (C) Fe 2p, and (D) Ti 2p.

2p spectrum of M/P-10 is shown in Figure 5C, where two dominant peaks were found at 724.3 and 709.8 eV, assigned to Fe  $2p_{1/2}$  and Fe  $2p_{3/2}$ , respectively. The satellite peak at 713.8 eV (Figure 5C) corresponds to Fe<sup>III</sup> in MIL-100(Fe). 41,42 Notably, these peaks exhibit negative shifts in comparison with the bare MIL-100(Fe) crystal (Figure 5C), 42,43 which is attributable to the formation of Fe-O-Ti bonds at the interface. Further evidence of the Fe-O-Ti bonds can be found in the Ti 2p spectrum of M/P-10 (Figure 5D). Specifically, the peaks centered at 463.6 and 458.5 eV are consistent with characteristic states of Ti in bare TiO<sub>2</sub> (Figure 5D), 44 whereas, the extra peak at 457.6 eV is related to the Ti ions with increased outer electron cloud densities, as a sequence of the presence of Fe-O-Ti bonds. 45 The Fe-O-Ti bonds were likely formed during the growth of MIL-100(Fe) on the surface of TiO2, where partial Ti atoms were replaced by Fe atoms. This substitution would lead to significant modification of the band structure of TiO2 as demonstrated through the DFT calculations (Figure 6).

To clarify the underlying changes in electronic properties, the electron-density distributions and electronic density of states (DoS) of bare TiO2 (Figure 6A) and Fe-doped TiO2 (denoted as TiO<sub>2</sub>(Fe) hereafter, Fe/Ti = 1:20, Figure 6B) were calculated. As shown in Figure 6C,D, the DoS of bare TiO<sub>2</sub> and TiO<sub>2</sub>(Fe) are dominated by Ti and O, with the same energy gap ( $\sim$ 2.0 eV). The calculated energy gap is lower than the experimental energy band gap of  $TiO_2$  (3.0-3.2 eV), which is due to the limitations of DFT calculation (i.e., lack of derivative discontinuity and self-interaction error). 46 Notably, the doping Fe creates defect energy levels, dominated by Fe and O, near the valence band (VB) maximum of TiO2. Correspondingly, as shown in Figure 6E, the charge density around the Fe site is much lower than that of the bare TiO<sub>2</sub>. Such a difference in charge density was achieved by subtracting

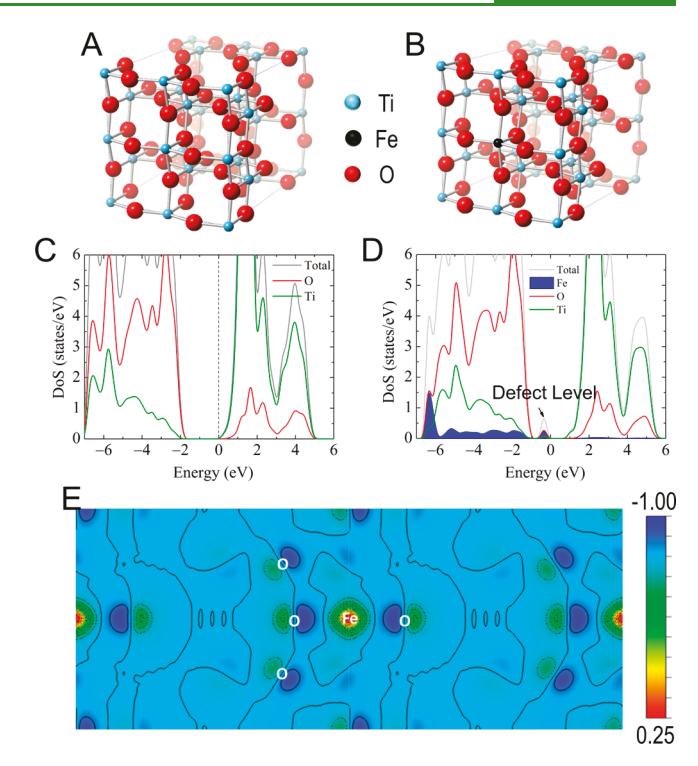


Figure 6. Optimized geometries of (A) TiO<sub>2</sub> and (B) TiO<sub>2</sub>(Fe), with Ti in blue, Fe in black, and O in red; (C) calculated DoS of the bare TiO2; (D) calculated DoS of TiO2(Fe); (E) calculated difference charge density (e/Bohr³) defined as the charge density of TiO<sub>2</sub>(Fe) subtracted by the charge density of bare TiO<sub>2</sub>. It shows that, around the Fe-doped site, the charge density is much smaller than that of the bare TiO2, corresponding to the peak of defect levels in DoS (D).

the charge density of bare TiO2 (Figure S4A) from that of TiO<sub>2</sub>(Fe) (Figure S4B). The defect energy levels would act as trappers of charge carriers to retard the excited electrons from recombining with holes, giving rise to increased amount of charge carriers in the composite system, which agrees well with TA results (Figure 4). On the other hand, the results are also consistent with those reported in prior studies where varied Fe/Ti ratios were used for DFT calculations, 47,48 which suggest that the DoS of the Fe-doped TiO2 would not change significantly over a reasonable range of Fe/Ti ratios. However, it should be noted that with excessive Fe doping, the defect energy levels will work as the recombination centers and thus reduce the photocatalytic efficiency,<sup>49</sup> which partially explains the decreased photocatalytic efficiency with a further increased amount of MIL-100(Fe).

Proposed Mechanism. On the basis of the aforementioned results and discussions, a reasonable mechanism (Scheme 2) was proposed to explain the enhanced photocatalytic performance achieved by the MIL-100(Fe)/TiO<sub>2</sub> composite. The growth of MIL-100(Fe) on the TiO2 surface caused partial substitution of Ti by Fe, which led to charge deficiency at the substitution region (Figure 6E). From the perspective of the electronic band structure, the Fe doping would result in defect energy levels (Figure 6D), which would trap excited electrons and prevent the electrons from recombining with the holes (Figure 4). Accordingly, the separation of the charge carriers was greatly promoted. It should be noted that the doped Fe would also facilitate the photocatalytic efficiency through the Fe<sup>3+</sup>/Fe<sup>2+</sup> redox cycle. To be specific, the doped Fe<sup>3+</sup> would be reduced to Fe<sup>2+</sup> by the

Scheme 2. Proposed Pathways of the Charge Transfer Inside MIL-100(Fe)/TiO<sub>2</sub> upon Light Irradiation

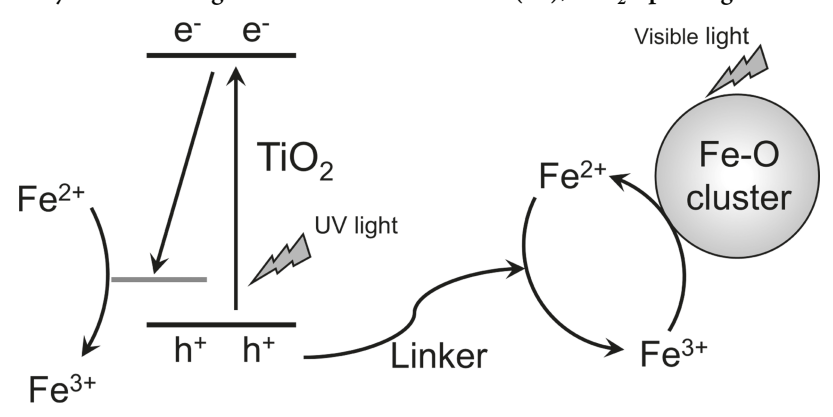


photo-induced electron as monitored by using electron spin resonance spectroscopy in prior studies.  $^{50,51}$  Subsequently, the Fe<sup>2+</sup> could not only improve the photooxidation process by providing more reactive oxygen species (eq 3) but also serve as a reductant to convert Cr(VI) to less toxic Cr(III) (eq 4).

$$Fe^{2+} + H_2O_2 \rightarrow Fe^{3+} + {}^{\bullet}OH + OH^-$$
 (3)

$$6Fe^{2+} + Cr_2O_7^{2-} + 14H^+ \rightarrow 6Fe^{3+} + 2Cr^{3+} + 7H_2O$$
(4

Furthermore, the intimate interaction between MIL-100(Fe) and TiO<sub>2</sub> also improves the charge separation (Scheme 2). Specifically, the incorporation of MIL-100(Fe) expanded the light absorption to the visible region (Figure 2E). Upon visiblelight irradiation, the Fe-O clusters in MIL-100(Fe) would be excited, during which the Fe3+ in MIL-100(Fe) would be reduced to Fe<sup>2+</sup> by accepting electrons from O<sup>2-.52</sup> Meanwhile, because of the intimate contact of MIL-100(Fe) and TiO<sub>2</sub>, holes in the TiO2 VB would migrate through the ligand to Fe-O clusters and oxidize Fe2+ back to Fe3+, which also contributes to the inhibition of charge recombination in TiO<sub>2</sub>.

In brief, the incorporated MIL-100(Fe) could enhance the charge separation of TiO2 by introducing defect energy levels and providing additional charge transfer pathways, which significantly increases the lifetimes of both electrons and holes. Besides, the doped Fe in the TiO2 structure would also promote the photocatalytic efficiency by offering additional reaction pathways through the Fe<sup>3+</sup>/Fe<sup>2+</sup> redox cycle.

## CONCLUSIONS

MIL-100(Fe)/P25 composite photocatalysts were fabricated and demonstrated better photocatalytic oxidation and reduction abilities over pristine P25. As evidenced by the ultrafast TA measurements, the enhanced photocatalytic performance is attributable to the promoted electron-hole separation because of the incorporation of MIL-100(Fe). In particular, partial Ti atoms were replaced with Fe atoms during the growth of MIL-100(Fe) on the TiO2 surface, which led to changes in electron-density distribution and created defect energy levels. During the photocatalytic process, the excited electrons would be captured at the defect energy levels, which greatly restrains the recombination of charge carriers and increases the amount of charge carriers, and thus, contributes to improved photocatalytic efficiency. Besides, the intimate interaction between MIL-100(Fe) and TiO2 provided an additional pathway to further improve the charge separation. Besides the promoted charge separation, the doped Fe in the

TiO<sub>2</sub> structure also boosted the photocatalytic efficiency through the Fe<sup>3+</sup>/Fe<sup>2+</sup> redox cycle. This work offers new insights into the interface structure of the MOF/semiconductor and its role in charge transfer, which would contribute to the future design of innovative MOF/semiconductor composite photocatalysts.

## ASSOCIATED CONTENT

## S Supporting Information

The Supporting Information is available free of charge on the ACS Publications website at DOI: 10.1021/acsami.9b00223.

Synthesis of pure MIL-100(Fe); FT-IR spectrum and PXRD pattern of P25 embedded by FeOOH; SEM-EDX spectrum of M/P-10; and electron-density distribution (PDF)

## AUTHOR INFORMATION

### **Corresponding Author**

\*E-mail: wnwang@vcu.edu. Phone: 1-(804) 827-4306. Fax: 1-(804) 827-7030.

## ORCID ®

Hong Fang: 0000-0002-0968-8687 David J. Gosztola: 0000-0003-2674-1379 Puru Jena: 0000-0002-2316-859X

Wei-Ning Wang: 0000-0002-1935-6301

The authors declare no competing financial interest.

## **ACKNOWLEDGMENTS**

We are very grateful for the financial support from National Science Foundation (CMMI-1727553). This work was performed, in part, at the Center for Nanoscale Materials (CNM) and the Advanced Photon Source (APS), U.S. Department of Energy Office of Science User Facilities operated by Argonne National Laboratory, and supported by the U.S. Department of Energy, Office of Science, under contract no. DE-AC02-06CH11357.

## REFERENCES

- (1) James, S. L. Metal-Organic Frameworks. Chem. Soc. Rev. 2003, 32, 276-288.
- (2) Stock, N.; Biswas, S. Synthesis of Metal-Organic Frameworks (MOFs): Routes to Various MOF Topologies, Morphologies, and Composites. Chem. Rev. 2012, 112, 933-969.

- (3) Drout, R. J.; Robison, L.; Farha, O. K. Catalytic Applications of Enzymes Encapsulated in Metal-Organic Frameworks. Coord. Chem. Rev. 2019, 381, 151-160.
- (4) Islamoglu, T.; Ray, D.; Li, P.; Majewski, M. B.; Akpinar, I.; Zhang, X.; Cramer, C. J.; Gagliardi, L.; Farha, O. K. From Transition Metals to Lanthanides to Actinides: Metal-Mediated Tuning of Electronic Properties of Isostructural Metal-Organic Frameworks. Inorg. Chem. 2018, 57, 13246-13251.
- (5) Lu, G.; Hupp, J. T. Metal-Organic Frameworks as Sensors: A ZIF-8 Based Fabry-Pérot Device as a Selective Sensor for Chemical Vapors and Gases. J. Am. Chem. Soc. 2010, 132, 7832-7833.
- (6) Cacho-Bailo, F.; Caro, G.; Etxeberría-Benavides, M.; Karvan, O.; Téllez, C.; Coronas, J. High Selectivity ZIF-93 Hollow Fiber Membranes for Gas Separation. Chem. Commun. 2015, 51, 11283-
- (7) Altintas, C.; Avci, G.; Daglar, H.; Nemati Vesali Azar, A.; Velioglu, S.; Erucar, I.; Keskin, S. Database for CO<sub>2</sub> Separation Performances of MOFs Based on Computational Materials Screening. ACS Appl. Mater. Interfaces 2018, 10, 17257-17268.
- (8) Hwang, Y. K.; Hong, D.-Y.; Chang, J.-S.; Jhung, S. H.; Seo, Y.-K.; Kim, J.; Vimont, A.; Daturi, M.; Serre, C.; Férey, G. Amine Grafting on Coordinatively Unsaturated Metal Centers of Mofs: Consequences for Catalysis and Metal Encapsulation. Angew. Chem., Int. Ed. 2008, 47, 4144-4148.
- (9) Kou, J.; Sun, L.-B. Fabrication of Metal-Organic Frameworks inside Silica Nanopores with Significantly Enhanced Hydrostability and Catalytic Activity. ACS Appl. Mater. Interfaces 2018, 10, 12051-12059.
- (10) Lu, G.; Li, S.; Guo, Z.; Farha, O. K.; Hauser, B. G.; Qi, X.; Wang, Y.; Wang, X.; Han, S.; Liu, X.; DuChene, J. S.; Zhang, H.; Zhang, Q.; Chen, X.; Ma, J.; Loo, S. C. J.; Wei, W. D.; Yang, Y.; Hupp, J. T.; Huo, F. Imparting Functionality to a Metal-organic Framework Material by Controlled Nanoparticle Encapsulation. Nat. Chem. 2012,
- (11) Müller, M.; Hermes, S.; Kähler, K.; van den Berg, M. W. E.; Muhler, M.; Fischer, R. A. Loading of MOF-5 with Cu and Zno Nanoparticles by Gas-Phase Infiltration with Organometallic Precursors: Properties of Cu/ZnO@MOF-5 as Catalyst for Methanol Synthesis. Chem. Mater. 2008, 20, 4576-4587.
- (12) He, X.; Wang, W.-N. Mof-Based Ternary Nanocomposites for Better CO<sub>2</sub> Photoreduction: Roles of Heterojunctions and Coordinatively Unsaturated Metal Sites. J. Mater. Chem. A 2018, 6, 932-
- (13) He, X.; Yang, C.; Wang, D.; Gilliland, S. E., III; Chen, D.-R.; Wang, W.-N. Facile Synthesis of ZnO@ZIF Core-Shell Nanofibers: Crystal Growth and Gas Adsorption. CrystEngComm 2017, 19, 2445-
- (14) Qiu, J.; Zhang, X.; Feng, Y.; Zhang, X.; Wang, H.; Yao, J. Modified Metal-Organic Frameworks as Photocatalysts. Appl. Catal., B 2018, 231, 317-342.
- (15) Zeng, X.; Huang, L.; Wang, C.; Wang, J.; Li, J.; Luo, X. Sonocrystallization of ZIF-8 on Electrostatic Spinning TiO<sub>2</sub> Nanofibers Surface with Enhanced Photocatalysis Property through Synergistic Effect. ACS Appl. Mater. Interfaces 2016, 8, 20274-20282.
- (16) Wang, X.; Liu, J.; Leong, S.; Lin, X.; Wei, J.; Kong, B.; Xu, Y.; Low, Z.-X.; Yao, J.; Wang, H. Rapid Construction of Zno@ZIF-8 Heterostructures with Size-Selective Photocatalysis Properties. ACS Appl. Mater. Interfaces 2016, 8, 9080-9087.
- (17) Wang, R.; Gu, L.; Zhou, J.; Liu, X.; Teng, F.; Li, C.; Shen, Y.; Yuan, Y. Quasi-Polymeric Metal-Organic Framework UiO-66/g-C<sub>3</sub>N<sub>4</sub> Heterojunctions for Enhanced Photocatalytic Hydrogen Evolution under Visible Light Irradiation. Adv. Mater. Interfaces 2015, 2, 1500037.
- (18) Su, Y.; Zhang, Z.; Liu, H.; Wang, Y. Cd0.2Zn0.8S@UiO-66-NH<sub>2</sub> Nanocomposites as Efficient and Stable Visible-Light-driven Photocatalyst for H2 Evolution and CO2 Reduction. Appl. Catal., B 2017, 200, 448-457.
- (19) Zhao, X.; Zhang, Y.; Wen, P.; Xu, G.; Ma, D.; Qiu, P. NH<sub>2</sub>-MIL-125(Ti)/TiO<sub>2</sub> Composites as Superior Visible-Light Photo-

- catalysts for Selective Oxidation of Cyclohexane. Mol. Catal. 2018, 452, 175-183.
- (20) Zhang, B.; Zhang, J.; Tan, X.; Shao, D.; Shi, J.; Zheng, L.; Zhang, J.; Yang, G.; Han, B. MIL-125-NH2@TiO2 Core-Shell Particles Produced by a Post-Solvothermal Route for High-Performance Photocatalytic H2 Production. ACS Appl. Mater. Interfaces 2018, 10, 16418-16423.
- (21) Wang, H.; Yuan, X.; Wu, Y.; Zeng, G.; Dong, H.; Chen, X.; Leng, L.; Wu, Z.; Peng, L. In situ synthesis of In<sub>2</sub>S<sub>3</sub>@MIL-125(Ti) core-shell microparticle for the removal of tetracycline from wastewater by integrated adsorption and visible-light-driven photocatalysis. Appl. Catal., B 2016, 186, 19-29.
- (22) He, X.; Gan, Z.; Fisenko, S.; Wang, D.; El-Kaderi, H. M.; Wang, W.-N. Rapid Formation of Metal-Organic Frameworks (MOFs) Based Nanocomposites in Microdroplets and Their Applications for CO<sub>2</sub> Photoreduction. ACS Appl. Mater. Interfaces 2017, 9, 9688-
- (23) Li, R.; Hu, J.; Deng, M.; Wang, H.; Wang, X.; Hu, Y.; Jiang, H.-L.; Jiang, J.; Zhang, Q.; Xie, Y.; Xiong, Y. Integration of an Inorganic Semiconductor with a Metal-Organic Framework: A Platform for Enhanced Gaseous Photocatalytic Reactions. Adv. Mater. 2014, 26, 4783-4788.
- (24) He, J.; Yan, Z.; Wang, J.; Xie, J.; Jiang, L.; Shi, Y.; Yuan, F.; Yu, F.; Sun, Y. Significantly Enhanced Photocatalytic Hydrogen Evolution under Visible Light over CdS Embedded on Metal-Organic Frameworks. Chem. Commun. 2013, 49, 6761-6763.
- (25) Panneri, S.; Thomas, M.; Ganguly, P.; Nair, B. N.; Mohamed, A. P.; Warrier, K. G. K.; Hareesh, U. S. C3N4 Anchored ZIF 8 Composites: Photo-Regenerable, High Capacity Sorbents as Adsorptive Photocatalysts for the Effective Removal of Tetracycline from Water. Catal. Sci. Technol. 2017, 7, 2118-2128.
- (26) Liu, X.; Dang, R.; Dong, W.; Huang, X.; Tang, J.; Gao, H.; Wang, G. A Sandwich-like Heterostructure of TiO2 Nanosheets with MIL-100(Fe): A Platform for Efficient Visible-Light-Driven Photocatalysis. Appl. Catal., B 2017, 209, 506-513.
- (27) Kresse, G.; Furthmüller, J. Efficiency of Ab-Initio Total Energy Calculations for Metals and Semiconductors Using a Plane-Wave Basis Set. Comput. Mater. Sci. 1996, 6, 15-50.
- (28) Fang, H.; Zhou, J.; Jena, P. Super-Alkalis as Building Blocks of One-Dimensional Hierarchical Electrides. Nanoscale 2018, 10, 22963-22969.
- (29) Ishikawa, T.; Takeuchi, K.; Kandori, K.; Nakayama, T. Transformation of  $\gamma$ -FeOOH to  $\alpha$ -FeOOH in acidic solutions containing metal ions. Colloids Surf., A 2005, 266, 155-159.
- (30) Horcajada, P.; Surblé, S.; Serre, C.; Hong, D.-Y.; Seo, Y.-K.; Chang, J.-S.; Grenèche, J.-M.; Margiolaki, I.; Férey, G. Synthesis and Catalytic Properties of MIL-100(Fe), an Iron(III) Carboxylate with Large Pores. Chem. Commun. 2007, 2820-2822.
- (31) Petit, C.; Bandosz, T. J. Synthesis, Characterization, and Ammonia Adsorption Properties of Mesoporous Metal-Organic Framework (MIL(Fe))-Graphite Oxide Composites: Exploring the Limits of Materials Fabrication. Adv. Funct. Mater. 2011, 21, 2108-
- (32) He, X.; Nguyen, V.; Jiang, Z.; Wang, D.; Zhu, Z.; Wang, W.-N. Highly-Oriented One-Dimensional MOF-Semiconductor Nanoarrays for Efficient Photodegradation of Antibiotics. Catal. Sci. Technol. **2018**, 8, 2117-2123.
- (33) Wang, C.-C.; Du, X.-D.; Li, J.; Guo, X.-X.; Wang, P.; Zhang, J. Photocatalytic Cr(VI) Reduction in Metal-Organic Frameworks: A Mini-Review. Appl. Catal., B 2016, 193, 198-216.
- (34) Shi, L.; Wang, T.; Zhang, H.; Chang, K.; Meng, X.; Liu, H.; Ye, J. An Amine-Functionalized Iron(III) Metal-Organic Framework as Efficient Visible-Light Photocatalyst for Cr(VI) Reduction. Adv. Sci. 2015, 2, 1500006.
- (35) Wang, D.; Jia, F.; Wang, H.; Chen, F.; Fang, Y.; Dong, W.; Zeng, G.; Li, X.; Yang, Q.; Yuan, X. Simultaneously Efficient Adsorption and Photocatalytic Degradation of Tetracycline by Fe-Based MOFs. J. Colloid Interface Sci. 2018, 519, 273-284.

- (36) Yang, Q.; Zhao, Q.; Ren, S.; Lu, Q.; Guo, X.; Chen, Z. Fabrication of Core-Shell Fe<sub>3</sub>O<sub>4</sub>@MIL-100(Fe) Magnetic Microspheres for the Removal of Cr(VI) in Aqueous Solution. *J. Solid State Chem.* **2016**, 244, 25–30.
- (37) Fang, Y.; Wen, J.; Zeng, G.; Jia, F.; Zhang, S.; Peng, Z.; Zhang, H. Effect of Mineralizing Agents on the Adsorption Performance of Metal-Organic Framework MIL-100(Fe) Towards Chromium(VI). *Chem. Eng. J.* **2018**, 337, 532–540.
- (38) Long, R.; Mao, K.; Gong, M.; Zhou, S.; Hu, J.; Zhi, M.; You, Y.; Bai, S.; Jiang, J.; Zhang, Q.; Wu, X.; Xiong, Y. Tunable Oxygen Activation for Catalytic Organic Oxidation: Schottky Junction Versus Plasmonic Effects. *Angew. Chem.* **2014**, *126*, 3269–3273.
- (39) Liu, J.; Li, J.; Sedhain, A.; Lin, J.; Jiang, H. Structure and Photoluminescence Study of TiO<sub>2</sub> Nanoneedle Texture Along Vertically Aligned Carbon Nanofiber Arrays. *J. Phys. Chem. C* **2008**, *112*, 17127–17132.
- (40) Wang, L.; Wang, Z.; Wang, H.-Y.; Grinblat, G.; Huang, Y.-L.; Wang, D.; Ye, X.-H.; Li, X.-B.; Bao, Q.; Wee, A.-S.; Maier, S. A.; Chen, Q.-D.; Zhong, M.-L.; Qiu, C.-W.; Sun, H.-B. Slow Cooling and Efficient Extraction of C-Exciton Hot Carriers in MoS<sub>2</sub> Monolayer. *Nat. Commun.* **2017**, *8*, 13906.
- (41) Zhao, H.; Qian, L.; Lv, H.; Wang, Y.; Zhao, G. Introduction of a Fe $_3$ O $_4$  Core Enhances the Photocatalytic Activity of MIL-100(Fe) with Tunable Shell Thickness in the Presence of H $_2$ O $_2$ . ChemCatChem 2015, 7, 4148–4155.
- (42) Zhang, F.; Shi, J.; Jin, Y.; Fu, Y.; Zhong, Y.; Zhu, W. Facile Synthesis of MIL-100(Fe) under HF-Free Conditions and Its Application in the Acetalization of Aldehydes with Diols. *Chem. Eng. J.* **2015**, 259, 183–190.
- (43) Lv, H.; Zhao, H.; Cao, T.; Qian, L.; Wang, Y.; Zhao, G. Efficient Degradation of High Concentration Azo-Dye Wastewater by Heterogeneous Fenton Process with Iron-Based Metal-Organic Framework. J. Mol. Catal. A: Chem. 2015, 400, 81–89.
- (44) Cao, L.; Tang, F.; Fang, G. Preparation and Characteristics of Microencapsulated Palmitic Acid with TiO<sub>2</sub> Shell as Shape-Stabilized Thermal Energy Storage Materials. *Sol. Energy Mater. Sol. Cells* **2014**, *123*, 183–188.
- (45) Mou, F.; Xu, L.; Ma, H.; Guan, J.; Chen, D.-R.; Wang, S. Facile Preparation of Magnetic  $\gamma$ -Fe<sub>2</sub>O<sub>3</sub>/TiO<sub>2</sub> Janus Hollow Bowls with Efficient Visible-Light Photocatalytic Activities by Asymmetric Shrinkage. *Nanoscale* **2012**, *4*, 4650–4657.
- (46) Geng, W.; Liu, H.; Yao, X. Enhanced Photocatalytic Properties of Titania-Graphene Nanocomposites: A Density Functional Theory Study. *Phys. Chem. Chem. Phys.* **2013**, *15*, 6025–6033.
- (47) Yu, J.; Xiang, Q.; Zhou, M. Preparation, Characterization and Visible-Light-Driven Photocatalytic Activity of Fe-Doped Titania Nanorods and First-Principles Study for Electronic Structures. *Appl. Catal., B* **2009**, *90*, 595–602.
- (48) Yen, C.-C.; Wang, D.-Y.; Chang, L.-S.; Shih, H. C. Characterization and Photocatalytic Activity of Fe- and N-Co-Deposited TiO<sub>2</sub> and First-Principles Study for Electronic Structure. *I. Solid State Chem.* **2011**, *184*, 2053–2060.
- (49) Li, Z.; Shen, W.; He, W.; Zu, X. Effect of Fe-Doped TiO<sub>2</sub> Nanoparticle Derived from Modified Hydrothermal Process on the Photocatalytic Degradation Performance on Methylene Blue. *J. Hazard. Mater.* **2008**, *155*, 590–594.
- (50) Nishikawa, M.; Mitani, Y.; Nosaka, Y. Photocatalytic Reaction Mechanism of Fe(III)-Grafted TiO<sub>2</sub> Studied by Means of ESR Spectroscopy and Chemiluminescence Photometry. *J. Phys. Chem. C* **2012**, *116*, 14900–14907.
- (51) Ohno, T.; Miyamoto, Z.; Nishijima, K.; Kanemitsu, H.; Xueyuan, F. Sensitization of Photocatalytic Activity of S- or N-Doped TiO<sub>2</sub> Particles by Adsorbing Fe<sup>3+</sup> Cations. *Appl. Catal., A* **2006**, 302, 62–68.
- (52) Wang, D.; Wang, M.; Li, Z. Fe-Based Metal-Organic Frameworks for Highly Selective Photocatalytic Benzene Hydroxylation to Phenol. ACS Catal. 2015, 5, 6852–6857.

## **Supporting Information**

# Mechanistic Insight into Photocatalytic Pathways of MIL-100(Fe)/TiO<sub>2</sub> Composites

Xiang  $He,^{\dagger}$  Hong  $Fang,^{\ddagger}$  David J. Gosztola,  $^{\perp}$  Zhang Jiang,  $^{\prime\prime}$  Puru Jena,  $^{\ddagger}$  and Wei-Ning  $Wang^{*,\dagger}$ 

<sup>†</sup>Department of Mechanical and Nuclear Engineering, and <sup>‡</sup> Department of Physics, Virginia Commonwealth University, Richmond, Virginia 23219, United States

<sup>⊥</sup> Center for Nanoscale Materials, and "Advanced Photon Source, Argonne National Laboratory, Lemont, Illinois 60439, United States

## \*Corresponding Author

Wei-Ning Wang: Tel: 1-(804) 827-4306; Fax: 1-(804) 827-7030; Email: wnwang@vcu.edu

## S1. Synthesis of Pure MIL-100(Fe)

Iron nitrate nonahydrate (1.2122 g), trimesic acid (0.6935 g), and deionized water (25 mL) were mixed in a Teflon autoclave, which was then heated at 150 °C for 12 hours. After cooling down to room temperature, the as-prepared powders were collected and subsequently washed through centrifugation and dispersion by deionized water for two times and by methanol once. Finally, the powders were dried in a vacuum oven at 50 °C overnight.

The PXRD pattern of the as-prepared powders was shown in **Figure S1**, which agrees well with the simulated pattern of MIL-100(Fe) crystal, indicating the successful synthesis of the pure MIL-100(Fe) crystals.

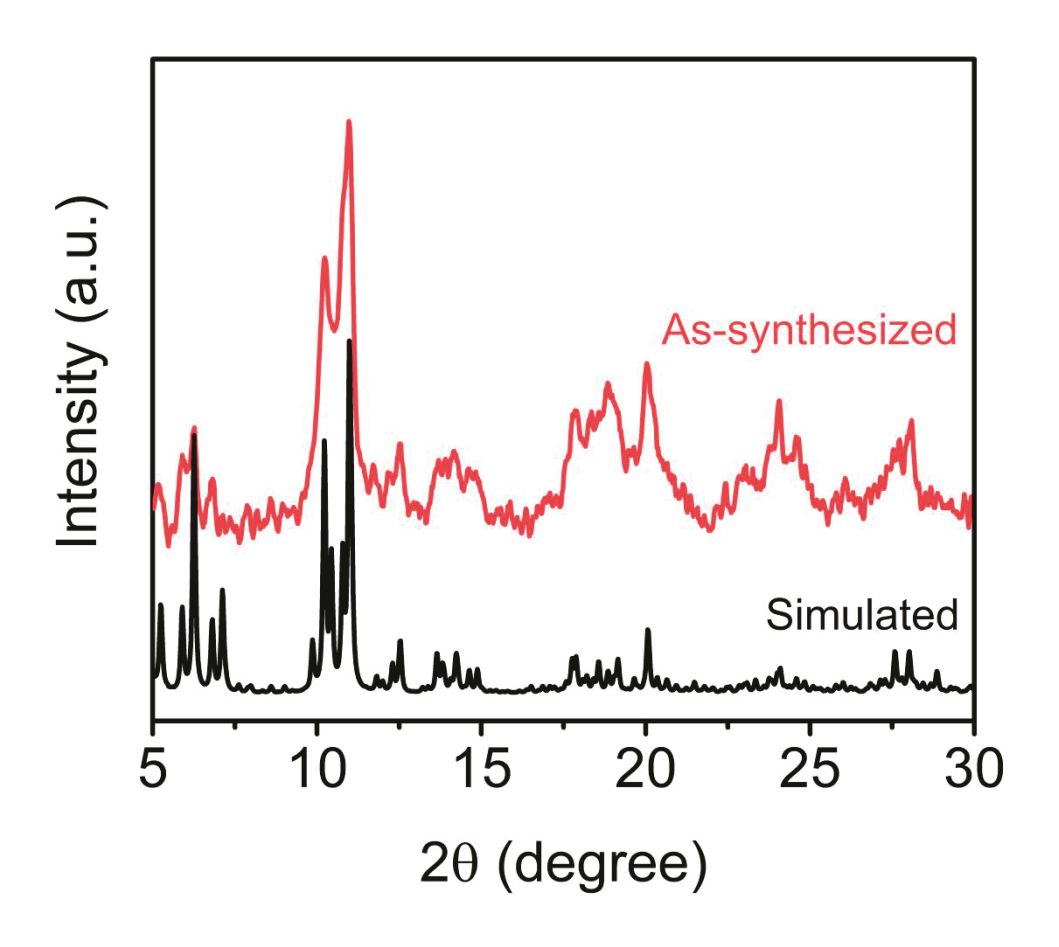
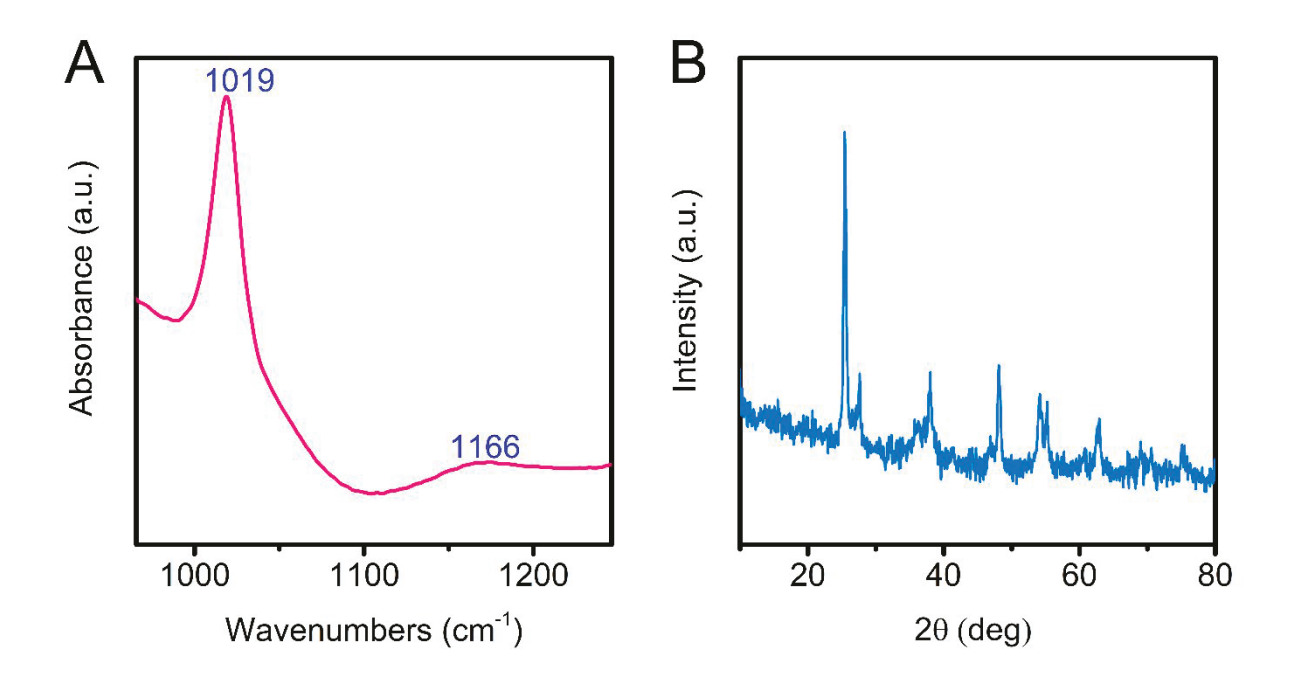


Figure S1. PXRD pattern of the pure MIL-100(Fe).

# S2. FT-IR Spectrum and PXRD Pattern of P25/FeOOH



**Figure S2**. (A) FT-IR spectrum and (B) PXRD pattern of P25 modified by 20 mM  $Fe(NO_3)_3 \cdot 9H_2O$ .

# S3. SEM-EDX Spectrum of M/P-10

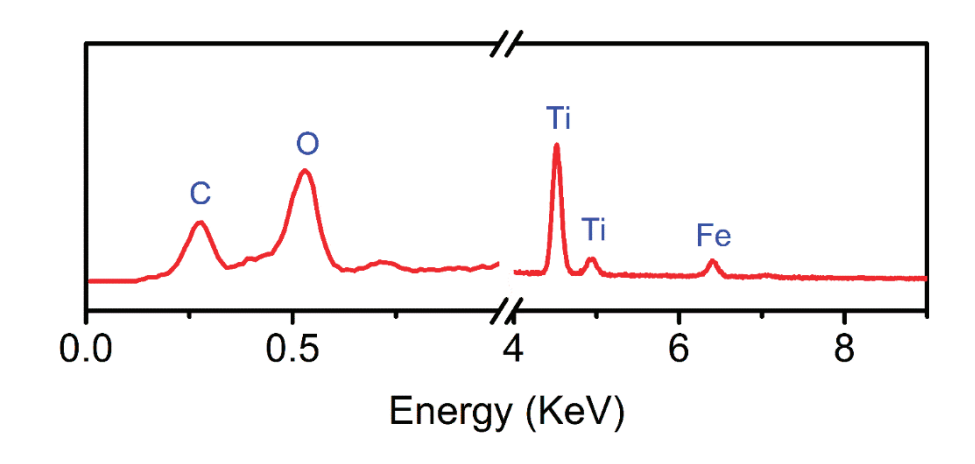
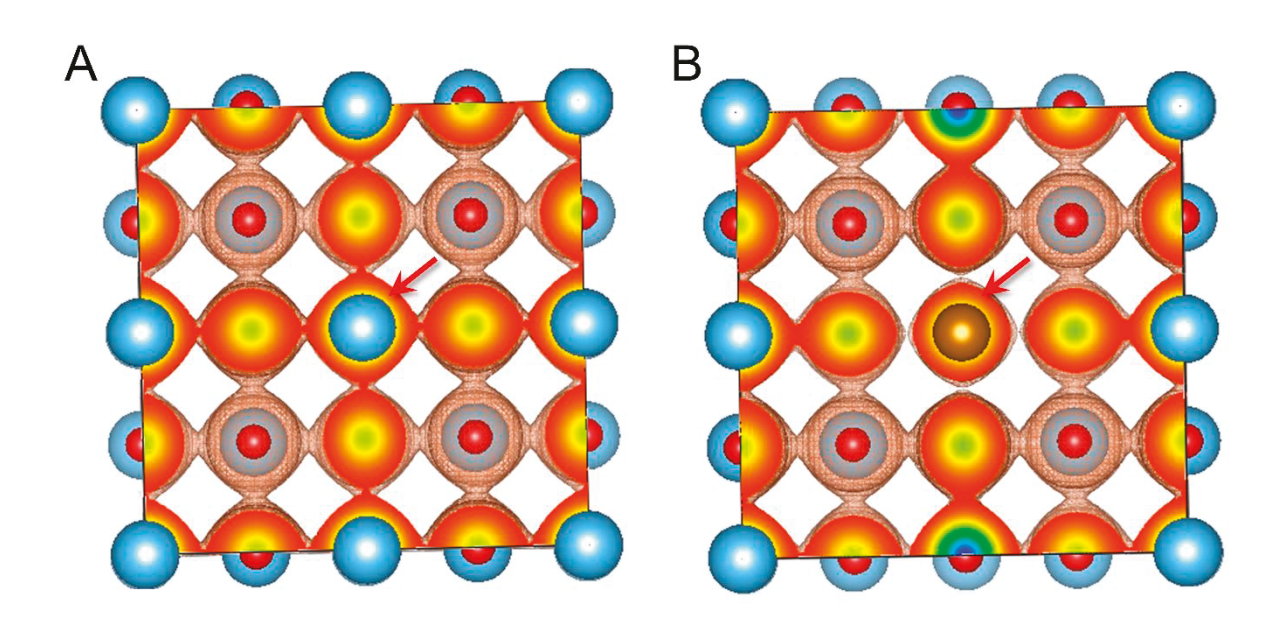


Figure S3. SEM-EDX spectrum of M/P-10.

# **S4.** Electron-Density Distributions



**Figure S4**. Electron-density distributions of (A) TiO<sub>2</sub> and (B) TiO<sub>2</sub>(Fe), with Ti in blue, O in red, Fe in brown.